

Simulations of magnetic fields in isolated disk galaxies

Rüdiger Pakmor¹ and Volker Springel^{1,2}

¹*Heidelberg Institut für Theoretische Studien, Schloss-Wolfsbrunnenvweg 35, 69118 Heidelberg, Germany*

²*Zentrum für Astronomie der Universität Heidelberg, Astronomisches Recheninstitut, Mönchhofstr. 12-14, 69120 Heidelberg, Germany*

27 November 2024

ABSTRACT

Magnetic fields are known to be dynamically important in the interstellar medium of our own Galaxy, and they are ubiquitously observed in diffuse gas in the halos of galaxies and galaxy clusters. Yet, magnetic fields have typically been neglected in studies of the formation of galaxies, leaving their global influence on galaxy formation largely unclear. Here we extend our magnetohydrodynamics (MHD) implementation in the moving-mesh code AREPO to cosmological problems which include radiative cooling and the formation of stars. In particular, we replace our previously employed divergence cleaning approach with a Powell 8-wave scheme, which turns out to be significantly more stable, even in very dynamic environments. We verify the improved accuracy through simulations of the magneto-rotational instability in accretion disks, which reproduce the correct linear growth rate of the instability. Using this new MHD code, we simulate the formation of isolated disk galaxies similar to the Milky Way using idealized initial conditions with and without magnetic fields. We find that the magnetic field strength is quickly amplified in the initial central starburst and the differential rotation of the forming disk, eventually reaching a saturation value. At this point, the magnetic field pressure in the interstellar medium becomes comparable to the thermal pressure, and a further efficient growth of the magnetic field strength is prevented. The additional pressure component leads to a lower star formation rate at late times compared to simulations without magnetic fields, and induces changes in the spiral arm structures of the gas disk. In addition, we observe highly magnetized fountain-like outflows from the disk. These results are robust with numerical resolution and are largely independent of the initial magnetic seed field strength assumed in the initial conditions, as the amplification process is rapid and self-regulated. Our findings suggest an important influence of magnetic fields on galaxy formation and evolution, cautioning against their neglect in theoretical models of structure formation.

Key words: methods: numerical, magnetohydrodynamics, galaxy formation

1 INTRODUCTION

Magnetic fields are ubiquitous in the Universe and appear to be present whenever ionized gas is involved. They are observed on vastly different scales, from the interiors of stars to interstellar gas, from haloes of galaxies to galaxy clusters (see, e.g., Parker 1979; Beck et al. 1996; Kulsrud 1999; Carilli & Taylor 2002; Govoni & Feretti 2004). There have even been claims of an indirect detection of magnetic fields in cosmic voids (Neronov & Vovk 2010), although the robustness of this result is debated (Broderick et al. 2012).

In galaxies, magnetic fields are suspected to be particularly important as here the magnetic pressure in the interstellar medium (ISM) becomes comparable to the thermal pressure. Magnetic fields may hence be dynamically relevant for the evolution of galaxies (Beck 2009), and for the regulation of their star formation. In addition, the structure

and strength of magnetic fields in galaxies determines the propagation of cosmic rays (e.g. Strong & Moskalenko 1998; Narayan & Medvedev 2001), which are another crucial ingredient influencing the gas dynamics of galaxies. In fact, the contribution of cosmic rays to the total pressure in the ISM is often assumed to be in equipartition with the magnetic field (Zweibel & Heiles 1997; Cox 2005), and the coupled dynamics of both components may be responsible for some of the galactic outflows (Ipavich 1975).

Magnetic field strengths have been measured for a number of galaxies using different methods, including Zeeman splitting in maser emission (Robishaw et al. 2008) and radio polarization measurements (see, e.g., Beck 2007). These observations provide us with quite detailed information about the magnetic field in the Milky Way (see, e.g., Jansson &

Farrar 2012a,b) and a few other nearby galaxies (e.g. Beck 2007).

However, it is still not well understood how galactic magnetic fields are originally generated and amplified, and which processes are most relevant for their evolution (for a recent review, see Kulsrud & Zweibel 2008). Weak initial magnetic fields could have a cosmological origin, or are created by Biermann batteries. A further amplification of these fields can then proceed through structure formation flows (e.g. Dolag et al. 1999), a Galactic Dynamo (e.g. Hanasz et al. 2004), or turbulent amplification (e.g. Arshakian et al. 2009). Since the amplification of the magnetic field in galaxies is strongly interwoven with the dynamical state of the gas, numerical simulations offer one of the best possibilities to study the complex magnetic field amplification and to clarify its role in regulating star formation on the scale of whole galaxies.

In clusters of galaxies, magnetic fields have been included in a number of cosmological simulations of cluster growth. Dolag et al. (1999, 2002) have shown that the complex shear flows and large adiabatic compression involved in building up the intracluster gas lead to a sizable amplification of magnetic fields, producing an end state that is largely insensitive to the initial seed field strength and configuration, and qualitatively matches observed Faraday rotation maps.

So far, only few high-resolution simulations of galaxy formation have attempted to include magnetic fields, largely owing to the technical challenges involved. Wang & Abel (2009) studied the evolution of magnetic fields in the formation of an isolated dwarf galaxy with radiative cooling, but without star formation. Dubois & Teyssier (2010) studied magnetic fields in dwarf galaxies including cooling and star formation, highlighting the dispersal of magnetic fields into the intergalactic medium (IGM) by supernova driven wind. These groups used a finite volume discretization of magnetohydrodynamics (MHD), but there have also been attempts to employ particle-based representations of MHD. In particular, Kotarba et al. (2009) compared two different MHD smoothed particle hydrodynamics (SPH) codes in simulations of magnetic field amplification in spiral galaxies. Kotarba et al. (2010, 2011) applied MHD-SPH techniques in studies of the magnetic field amplification in galaxy mergers, and Beck et al. (2012) employed SPH to simulate the evolution of the magnetic field in a Milky Way-like halo embedded in a cosmological environment. However, the latter study focussed on predictions for the diffuse gas in the galactic halo and did not discuss the properties of the magnetic field on the scale of the gaseous disk.

In this paper, we aim to investigate the role of magnetic fields in the evolution of Milky Way-sized galaxies, including the regime where magnetic forces become dynamically important in the dense ISM gas. We shall focus on idealized isolated galaxy models in this work, in preparation for future cosmological simulations of galaxy formation that include magnetic fields. Another goal of the present study lies in describing and demonstrating the technical improvements in our updated MHD solver, which now reaches an accuracy that allows it to solve difficult MHD hydrodynamical problems such as field amplification through the magnetorotational instability.

Accounting for ideal magnetohydrodynamics in the con-

text of galaxy formation simulations is technically challenging, primarily because of the well-known difficulties to maintain the $\nabla \cdot \mathbf{B} = 0$ constraint in simple discretization schemes, an issue which is especially severe in the light of the very large dynamic range and spatial adaptivity that is required in galaxy simulations. One of the best approaches to address this problem lies in constrained transport schemes coupled to adaptive mesh refinement (AMR). However, this technique also comes with disadvantages such as comparatively large advection errors for supersonic bulk flows, something quite common in cosmic structure formation. The moving-mesh code AREPO (Springel 2010) is a new approach that overcomes this limitation, but requires a more complicated unstructured mesh geometry. Recently, we presented a first implementation of MHD in the AREPO code (Pakmor et al. 2011), which combines the accuracy of mesh-based techniques for hydrodynamics with the automatic adaptivity and geometric flexibility of particle based techniques such as SPH. Here, we shall first begin by presenting an important improvement of our previous implementation of ideal MHD, as well as describing the required extensions for cosmological integration in comoving coordinates. We will also show validation tests of the technique that demonstrate that the $\nabla \cdot \mathbf{B}$ errors are kept under control and that complicated flows such as strong field amplification in shear flows are calculated correctly. This method is then applied to simulations of isolated galaxy models, with and without magnetic fields.

This paper is structured as follows. In Section 2, we describe the technical implementation of our improved MHD solver. In Section 3 we apply our code to simulate a magnetized accretion disk and compare the linear growth of the magneto-rotational instability to the analytical solution and the results of previous work in the literature. In Section 4, we briefly summarize the implementation of cooling, star formation, and associated feedback in our runs, and we specify our initial conditions. Section 5 is devoted to a discussion of our primary results for high-resolution simulations of isolated Milky Way-sized dark matter halos with and without magnetic fields. Finally, we give a summary and discussion of our findings in Section 6.

2 MHD IMPLEMENTATION

2.1 Cosmological ideal magnetohydrodynamics

The equations of ideal MHD in physical coordinates \mathbf{r} are given by

$$\frac{\partial \rho}{\partial t} + \nabla_{\mathbf{r}} \cdot (\rho \mathbf{v}) = 0, \quad (1)$$

$$\frac{\partial \rho \mathbf{v}}{\partial t} + \nabla_{\mathbf{r}} \cdot (\rho \mathbf{v} \mathbf{v}^T + p_{\text{tot}} - \mathbf{B} \mathbf{B}^T) = 0, \quad (2)$$

$$\frac{\partial E}{\partial t} + \nabla_{\mathbf{r}} \cdot [\mathbf{v} (E + p_{\text{tot}}) - \mathbf{B} (\mathbf{v} \cdot \mathbf{B})] = 0, \quad (3)$$

$$\frac{\partial \mathbf{B}}{\partial t} + \nabla_{\mathbf{r}} \cdot (\mathbf{B} \mathbf{v}^T - \mathbf{v} \mathbf{B}^T) = 0. \quad (4)$$

The time derivatives are here defined at constant physical position \mathbf{r} , and the spatial derivatives in $\nabla_{\mathbf{r}}$ are defined with respect to \mathbf{r} . Here, $p_{\text{tot}} = p_{\text{gas}} + \frac{1}{2} \mathbf{B}^2$ is the total gas pressure, and $E = \rho u_{\text{th}} + \frac{1}{2} \rho \mathbf{v}^2 + \frac{1}{2} \mathbf{B}^2$ is the total energy per unit volume, with u_{th} denoting the thermal energy per unit

mass, ρ , \mathbf{v} and \mathbf{B} represent the local gas density, velocity and magnetic field strength, respectively.

In addition, the magnetic field \mathbf{B} has to fulfill the divergence constraint, $\nabla \cdot \mathbf{B} = 0$. Analytically, this constraint will automatically be met at all times if it is fulfilled by the initial magnetic field. Discretization errors, however, can lead to a non-vanishing divergence of the magnetic field in numerical simulations. We will discuss this issue and how we deal with it in Section 2.3.

2.2 Extending the MHD equations to comoving coordinates

For definiteness, we briefly discuss the formulation of the MHD equations adopted in our code for expanding space. In cosmological simulations, it is convenient and common practice to use spatial coordinates comoving with the expansion of the Universe, such that only gas motions relative to the local standard of rest need to be computed. As usual, we parametrize the global expansion of the Universe with the time-dependent scale-factor $a(t)$. Besides introducing comoving coordinates \mathbf{x} , we also define other ‘comoving’ variables (denoted with a ‘c’ index) for velocity, density, pressure, and magnetic field, as follows:

$$\mathbf{r} = a \mathbf{x}, \quad (5)$$

$$\mathbf{u} = \mathbf{v} - \dot{a} \mathbf{x}, \quad (6)$$

$$\rho = \rho_c a^{-3}, \quad (7)$$

$$p = p_c a^{-3}, \quad (8)$$

$$\mathbf{B} = \mathbf{B}_c a^{-2}. \quad (9)$$

Here $\mathbf{v} = \dot{\mathbf{r}}$ is the physical velocity, and \mathbf{u} the peculiar velocity. With the exception of the magnetic field, these replacements are the standard definitions, but different choices have been used in the literature to define \mathbf{B}_c . The definition we adopt here has the advantage of avoiding a source term in the induction equation, as shown below.

The transformed equations in comoving coordinates based on these replacements are as follows:

$$\begin{aligned} \frac{\partial \rho_c}{\partial t} + \frac{1}{a} \nabla_{\mathbf{x}} \cdot (\rho_c \mathbf{u}) &= 0, \\ \frac{\partial \rho_c \mathbf{u}}{\partial t} + \frac{1}{a} \nabla_{\mathbf{x}} \cdot \left(\rho_c \mathbf{u} \mathbf{u}^T + p_{\text{tot},c} - \frac{\mathbf{B}_c \mathbf{B}_c^T}{a} \right) &= \\ = -\frac{\dot{a}}{a} \rho_c \mathbf{u}, \end{aligned} \quad (10)$$

$$\begin{aligned} \frac{\partial E_c}{\partial t} + \frac{1}{a} \nabla_{\mathbf{x}} \cdot [\mathbf{u} (E_c + p_{\text{tot},c}) - \mathbf{B}_c (\mathbf{u} \cdot \mathbf{B}_c)] &= \\ = -\frac{\dot{a}}{a} \left(\rho_c \mathbf{u}^2 + 2u_{\text{th}} + \frac{\mathbf{B}_c^2}{2a} \right), \end{aligned} \quad (11)$$

$$\frac{\partial \mathbf{B}_c}{\partial t} + \frac{1}{a} \nabla_{\mathbf{x}} \cdot (\mathbf{B}_c \mathbf{u}^T - \mathbf{u} \mathbf{B}_c^T) = 0. \quad (12)$$

Now the time derivatives are defined at constant comoving position \mathbf{x} and the spatial derivatives in $\nabla_{\mathbf{x}}$ are defined with respect to \mathbf{x} . We also introduced the total comoving pressure $p_{\text{tot},c} = p_{\text{gas}} + \frac{1}{2a} \mathbf{B}_c^2$ and the total comoving energy density per unit volume, $E_c = \rho_c u_{\text{th}} + \frac{1}{2} \rho_c \mathbf{u}^2 + \frac{1}{2a} \mathbf{B}_c^2$.

To get rid of most of the source terms we finally introduce scaled variables for the momentum and energy, viz.

$$\mathbf{w} = a \mathbf{u}, \quad (13)$$

$$\mathcal{E} = a^2 E_c. \quad (14)$$

Substituting these new variables into the cosmological MHD equations leads to the conservative system we actually solve in our code:

$$\frac{\partial \rho_c}{\partial t} + \frac{1}{a} \nabla_{\mathbf{x}} \cdot (\rho_c \mathbf{u}) = 0, \quad (15)$$

$$\frac{\partial \rho_c \mathbf{w}}{\partial t} + \nabla_{\mathbf{x}} \cdot \left(\rho_c \mathbf{u} \mathbf{u}^T + p_{\text{tot},c} - \frac{\mathbf{B}_c \mathbf{B}_c^T}{a} \right) = 0, \quad (16)$$

$$\frac{\partial \mathcal{E}}{\partial t} + a \nabla_{\mathbf{x}} \cdot \left[\mathbf{u} (E_c + p_{\text{tot},c}) - \frac{1}{a} \mathbf{B}_c (\mathbf{u} \cdot \mathbf{B}_c) \right] = \frac{\dot{a}}{2} \mathbf{B}_c^2, \quad (17)$$

$$\frac{\partial \mathbf{B}_c}{\partial t} + \frac{1}{a} \nabla_{\mathbf{x}} \cdot (\mathbf{B}_c \mathbf{u}^T - \mathbf{u} \mathbf{B}_c^T) = 0. \quad (18)$$

Note that in these equations only one source term remains as part of the energy equation.

The above equations have a similar form as the ordinary MHD equations (1) in fixed coordinates, and in fact reduce to them for $a(t) = 1$, as expected. Note that we can use a normal Riemann solver to calculate the fluxes without the need for cosmological adjustments, using the following procedure:

(i) We reconstruct the comoving primitive variables for a cell-interface in its rest-frame, using the MUSCL-Hancock approach as described in Springel (2010).

(ii) We scale the magnetic field as $\mathbf{B}'_c = \mathbf{B}_c / \sqrt{a}$.

(iii) We then calculate the fluxes across the moving interface from the reconstructed primitive variables and \mathbf{B}'_c using the HLLD riemann solver (Miyoshi & Kusano 2005), as described in Pakmor et al. (2011).

(iv) We finally revert the scaling of the magnetic field fluxes using $\mathbf{F}_B = \mathbf{F}'_B \times \sqrt{a}$, and multiply all other fluxes with the appropriate powers of the scale factor a .

The source term in the energy equation (15) is treated in a Strang-split fashion by applying two half-timesteps before and after evolving the homogenous system by one step, similar as the treatment of the gravitational source terms.

2.3 The divergence constraint

Although the induction equation (18) analytically fulfills the divergence constraint of an initially divergence free magnetic field at all times, this property is usually lost for the discretized version of the induction equation. However, a magnetic field which develops a non-zero divergence can lead to severe artifacts in numerical simulations. In particular, divergence errors can induce a huge local amplification of the magnetic and velocity fields, rendering both unphysical.

An elegant solution to this problem is the constraint transport approach (Evans & Hawley 1988). This scheme discretizes magnetic and electric fields such that the sequence of their update steps manifestly guarantees a vanishing divergence of the magnetic field at cell centres, to machine precision. Unfortunately, however, this method is at present limited to Cartesian grids, and it is conceptually unclear whether it can be adapted to unstructured moving meshes at all.

Instead of trying to completely avoid divergence errors by construction, as in constraint transport, we therefore attempt to keep them as small as possible, so that they do not affect our results. In Pakmor et al. (2011) we implemented the Dedner divergence cleaning approach (Dedner

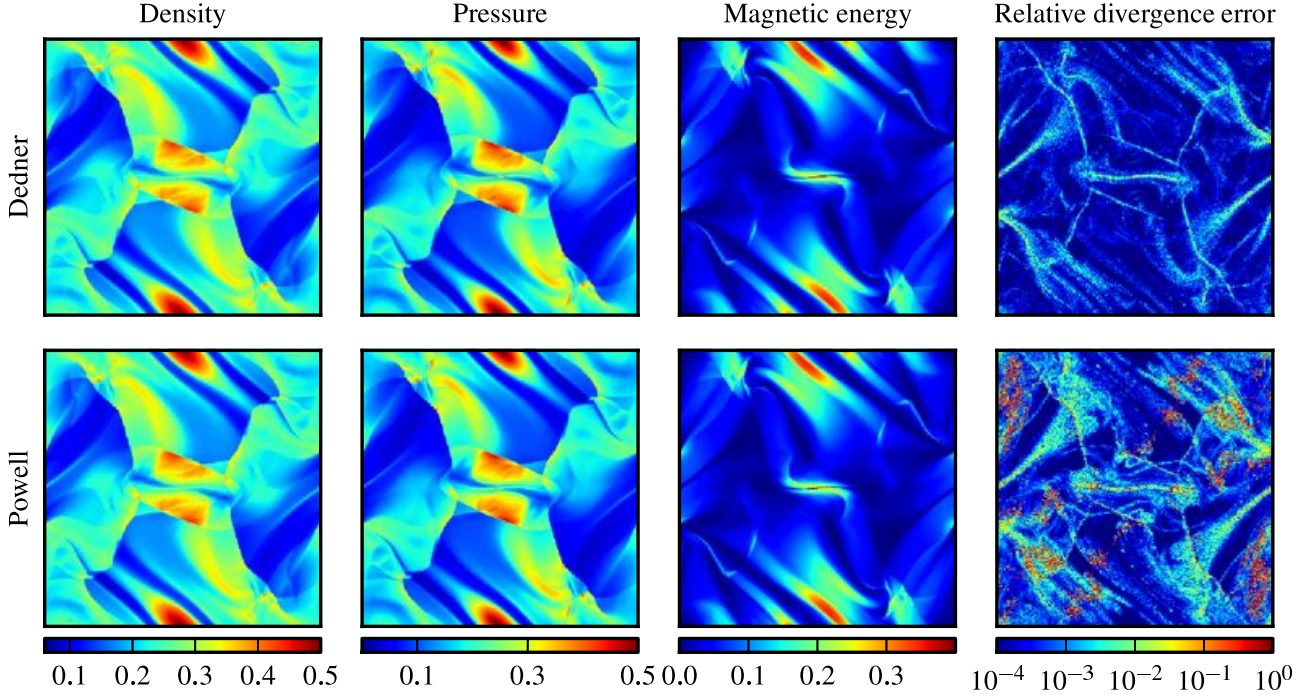


Figure 1. Orszag-Tank vortex at $t = 0.5$ for the Dedner divergence cleaning (top row) and the Powell scheme (bottom row). Shown from left to right are density, pressure, magnetic energy, and the absolute value of the relative divergence error as defined in Eqn. (23). Both simulations were run with 600×600 cells.

et al. 2002) in the moving-mesh code AREPO and showed that it is usually able to keep the divergence error at a small level. In the Dedner scheme, a local divergence error is both advected away from the place where it originates and also damped at the same time. However, as shown in Pakmor et al. (2011), a relatively restrictive timestep criterion is required to use the Dedner scheme together with individual timesteps for the cells, and even then it is difficult to guarantee stability in very dynamic environments, encumbering applications to cosmic structure formation.

To remedy these issues, we now adopt the Powell approach for divergence control (Powell et al. 1999). In this scheme, additional source terms are introduced into the momentum equation, induction equation and energy equation:

$$\frac{\partial \rho_c}{\partial t} + \frac{1}{a} \nabla_x \cdot (\rho_c \mathbf{u}) = 0, \quad (19)$$

$$\begin{aligned} \frac{\partial \rho_c \mathbf{w}}{\partial t} + \nabla_x \cdot \left(\rho_c \mathbf{u} \mathbf{u}^T + p_{\text{tot},c} - \frac{\mathbf{B}_c \mathbf{B}_c^T}{a} \right) = \\ - \frac{1}{a} (\nabla_x \cdot \mathbf{B}_c) \mathbf{B}_c, \end{aligned} \quad (20)$$

$$\begin{aligned} \frac{\partial \mathcal{E}}{\partial t} + a \nabla_x \cdot \left[\mathbf{u} (E_c + p_{\text{tot},c}) - \frac{1}{a} \mathbf{B}_c (\mathbf{u} \cdot \mathbf{B}_c) \right] = \\ \frac{\dot{a}}{2} \mathbf{B}_c^2 - \frac{1}{a} (\nabla_x \cdot \mathbf{B}_c) (\mathbf{u} \cdot \mathbf{B}_c), \end{aligned} \quad (21)$$

$$\frac{\partial \mathbf{B}_c}{\partial t} + \frac{1}{a} \nabla_x \cdot (\mathbf{B}_c \mathbf{u}^T - \mathbf{u} \mathbf{B}_c^T) = - \frac{1}{a} (\nabla_x \cdot \mathbf{B}_c) \mathbf{u}. \quad (22)$$

These source terms encode a passive advection of $\nabla \cdot \mathbf{B} / \rho$ with the flow and counteract further growth of local $\nabla \cdot \mathbf{B}$ errors. By experience, we find that this scheme is very stable in practical applications. A welcome advantage is also that it is completely local and does not require any additional

constraints on the timesteps, even when all cells are evolved on individual timesteps.

We apply the divergence source terms for all active cells at the same time when we calculate and apply the local fluxes. In each timestep, we first define the magnetic field perpendicular to a cell interface as the average of the perpendicular magnetic fields left and right of the interface, $B_x = \frac{1}{2} (B_{x,L} + B_{x,R})$. This value of B_x is then used in the Riemann solver. We estimate the divergence of the magnetic field of an active Voronoi cell by

$$\nabla \cdot \mathbf{B}_i = \frac{1}{V_i} \sum_{\text{faces}} \mathbf{B} \cdot \hat{\mathbf{n}} A_i, \quad (23)$$

using the average normal component B_x at the interfaces calculated as above, and add the fluxes and divergence source terms at the same time to our conservative variables. To estimate the relative size of the divergence error, we typically also use the values for the divergence of the magnetic field calculated as part of this treatment of the source terms.

2.4 Testing the divergence control

As one important test of our new implementation of divergence control based on the Powell approach, we simulate the Orszag-Tang vortex problem with the same configuration as shown in Pakmor et al. (2011), using both the previously implemented Dedner divergence cleaning and the Powell approach. The two simulations are shown at time $t = 0.5$ in Fig. 1, for comparison. There is excellent agreement between both results in density, pressure and magnetic energy, although the employed approach to limit divergence errors is significantly different. Note that this agreement is

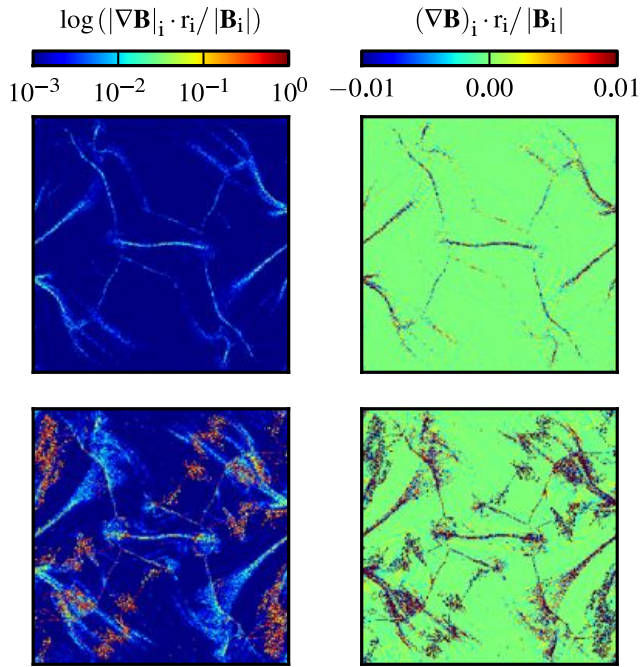


Figure 2. Maps of the divergence error for a Orszag-Tank vortex at $t = 0.5$ for the Dedner divergence cleaning (top row) and the Powell scheme (bottom row). The left column shows the absolute value of the relative magnetic divergence error on a logarithmic scale, whereas the right column shows its signed value on a linear scale. Both simulations were run with 600×600 cells.

a non-trivial outcome, given that small and seemingly innocent changes in the implementation details of each of the divergence control methods are typically readily punished by clearly visible artifacts in these physical quantities. This is because both approaches are intricate numerical schemes that just barely keep the $\nabla \cdot \mathbf{B}$ related errors under control.

There are, however, some differences in the relative size of the resulting divergence errors. As is clearly visible in Fig. 1, the absolute value of the relative divergence error is larger in some regions for the Powell approach compared to the Dedner divergence cleaning. This is visible even better in Fig. 2, where maps of the divergence error are shown. At time $t = 0.5$, we find a volume-weighted average of the magnitude of the relative divergence error equal to 9×10^{-4} for the Dedner divergence cleaning, and 2.4×10^{-2} for the Powell approach, respectively. If the sign of the divergence error is not ignored in the averaging, the mean divergence error is much smaller, only -3×10^{-5} for the Dedner scheme and -2×10^{-4} for the Powell method, because positive and negative fluctuations in $\nabla \cdot \mathbf{B}$ tend to largely cancel.

It is important to note that for both measurement methods the average relative divergence error is much smaller than unity and spatially highly localized. The spatial distribution of the errors is very similar for both divergence cleaning schemes. Interestingly, in places where the absolute value of the relative divergence error becomes large, its sign alternates between neighboring cells. This suggests that the divergence error occurs as a locally confined problem, most likely originating in approximate solutions of the Riemann problems and in the local discretization and truncation er-

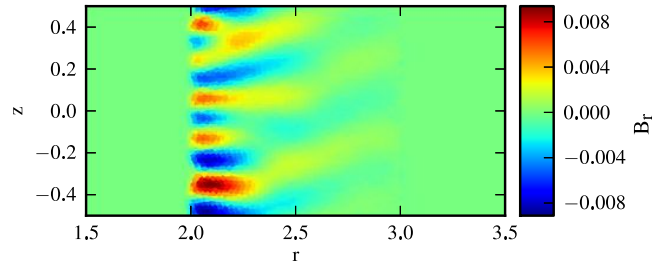


Figure 3. Radial magnetic field at $t = 30$ for a test of the magneto-rotational instability, after about five inner orbits.

rors. The local errors are oscillatory in nature, and the partial cancellation among neighboring cells helps to keep any large-scale impact very small. Although the average divergence error is about an order of magnitude larger for the Powell scheme compared to the Dedner cleaning, there are no noticeable differences in any fluid quantities, as shown in Fig. 1, supporting this interpretation. This good alignment of the two schemes in the Orszag-Tang vortex problem is only lost at much later time, when the initial vortex has decayed into turbulence, and the turbulent state as a function of time becomes slightly different between the schemes. In Sec. 5.7, we will return to a discussion of the divergence error in our applications of the code to realistic galaxy simulation.

3 MAGNETO-ROTATIONAL INSTABILITY

The magneto-rotational instability (MRI) (Balbus & Hawley 1991) is one of the most important MHD phenomena in astrophysics, making it a critical test-problem for numerical MHD codes. In particular, in accretion disks the MRI is suspected to provide the primary means for an efficient transport of angular momentum in the radial direction, allowing the gas to be accreted by the central compact object. The MRI may also facilitate the growth of magnetic fields in galaxies (Kitchatinov & Rüdiger 2004). Interestingly, for accretion disks it is possible to calculate the linear growth rate of the MRI analytically (Balbus & Hawley 1991), allowing for a direct quantitative check of whether a numerical MHD implementation can correctly account for this process.

3.1 Test setup

We employ the same setup as used in Flock et al. (2010), but simulate the full disk to avoid the need for azimuthal boundary conditions. In this setup, a thin, non self-gravitating, Keplerian disk rotates around a central body of unit mass, $M = 1$, implying a centripetal acceleration of $g(R) = 1/R^2$ in cylindrical coordinates. The disk extends from $R = 1$ to $R = 4$ in radial direction and from $z = -0.5$ to $z = 0.5$ in vertical direction. Initially, it has uniform density $\rho = 1$ and pressure $P = c_s^2 \rho / \gamma$, with $c_s = 0.1$ and $\gamma = 5/3$, and rotates with an azimuthal velocity of $v_\phi = \sqrt{1/R}$. The radial and vertical velocity is given by axisymmetric random perturbations of amplitude $\pm 5 \times 10^{-4}$.

A uniform vertical magnetic field with a strength of $0.05513/n$ and $n = 4$ pervades the disk between the radii $R = 2$ and $R = 3$. We use periodic boundary conditions in the vertical direction and a layer of boundary cells at $R = 1$

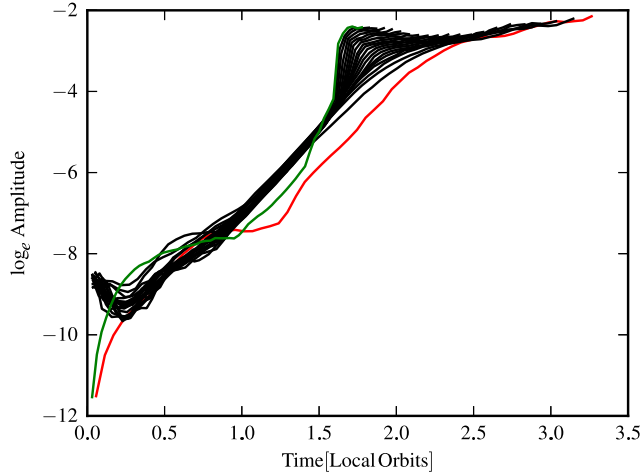


Figure 4. Maximal amplitude of the radial magnetic field at 21 equally spaced radii from $R = 2$ to $R = 3$ versus local orbits. The red and green line show the amplitude at radii $R = 2$ and $R = 3$, respectively.

and $R = 4$. These boundary cells keep the undisturbed parts of the disk at their initial radial position.

The mesh-generating points are initially arranged on 128 circular rings in the plane of rotation and duplicated 64 times uniformly in the vertical direction. The number of cells per ring is set such that cells have a mass of $\approx 10^{-5}$ per cell, with a uniform spacing within each ring.

For this setup, the radial and azimuthal magnetic field should be amplified exponentially in time according to $B = B_0 \exp(\gamma_{\text{MRI}} t)$ (Balbus & Hawley 1991). The fastest-growing mode in vertical direction should be the $n = 4$ mode, the dominant radial mode depends on the initial perturbations. The critical (fastest possible) mode grows with $\gamma_{\text{MRI}} = 0.75\Omega$, with an angular frequency $\Omega = R^{-1.5}$ as a function of radius.

3.2 Results

Figure 3 shows the radial magnetic field after about 5 inner orbits, corresponding to 1.8 orbits at $R = 2$. The MRI is clearly active and a radial magnetic field has emerged. The dominant vertical mode of the instability is close to $n = 4$, as predicted for this setup. The magnetic field is largest at $R = 2$ and becomes smaller with increasing radius (for the pattern, compare to Flock et al. 2010). We note that the “checkerboard”-instability that occurs for some implementations tested in Flock et al. (2010) does not show up in our simulation.

The growth of the amplitude of the radial magnetic field at different radii is shown in Fig. 4. Between about 0.5 and 1.5 local orbits, the amplitude increases exponentially, essentially at all radii. Only the very inner and outer radii at $R = 2$ and $R = 3$ are slightly different, most likely due to boundary effects. Starting after about 1.5 local orbits, the growth becomes steeper at a progressively larger range of radii, since the magnetic field is already saturated in the inner parts of the disk, which leads to non-linear growth in regions close to the saturated part.

We fit the growth rate at different radii selected be-

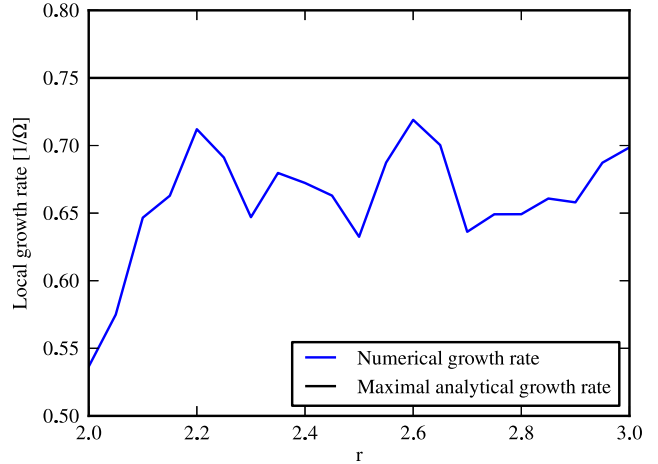


Figure 5. Exponential growth rate of the magnetic field amplitude measured at different radii (blue line). The black line shows the maximum growth rate expected analytically.

tween 1.0 and 1.5 local orbits and show the result in Fig. 5. The growth rate in units of the inverse orbital period ranges from 0.53 to 0.72 at different radii with an average growth rate of 0.66, in very good agreement with the results by Flock et al. (2010) for the same setup, which were based on completely different MHD implementations that included constraint transport. Also, there are no regions in our results where the local growth rate exceeds the fastest possible growth rate of 0.75. Reassuringly, we thus conclude that our code is able to correctly reproduce the linear phase of the magneto-rotational instability.

4 SIMULATION SETUP AND ADDITIONAL PHYSICS

Our disk galaxy simulations start from slowly rotating spherical gas clouds embedded in equilibrium into a collisionless dark matter halo (using the setup of Jubelgas et al. 2008). The dark matter halo is modelled with a static background potential corresponding to a NFW density profile (Navarro et al. 1997) with a mass of $M_{200} = 10^{12} M_{\odot}$ and a concentration parameter of 7.2 roughly resembling the halo of the Milky Way. We employ a spin parameter of $\lambda = 0.05$ and a baryonic mass fraction of 0.17. In the simulations with magnetic fields, we typically introduce a homogeneous seed magnetic field of 10^{-9} G parallel to the x -axis. The same or similar seed field strengths have also been used by Wang & Abel (2009), Kotarba et al. (2009) and Dubois & Teyssier (2010). Indeed, intergalactic fields of this size are expected in models of IGM magnetic seeding through outflows from dwarf galaxies at high redshift (Kronberg et al. 1999). Nevertheless, we have also varied the strength of the seed field in a subset of our tests.

Gravitational forces are calculated with a standard tree-method (based on Barnes & Hut 1986; Springel 2005) to account for the self-gravity of the gas. The forces due to dark matter are determined from the static background potential, neglecting a possible the adiabatic contraction of the halo when baryons cool and settle in the centre. We use the AREPO code in its pseudo-Lagrangian configuration for our

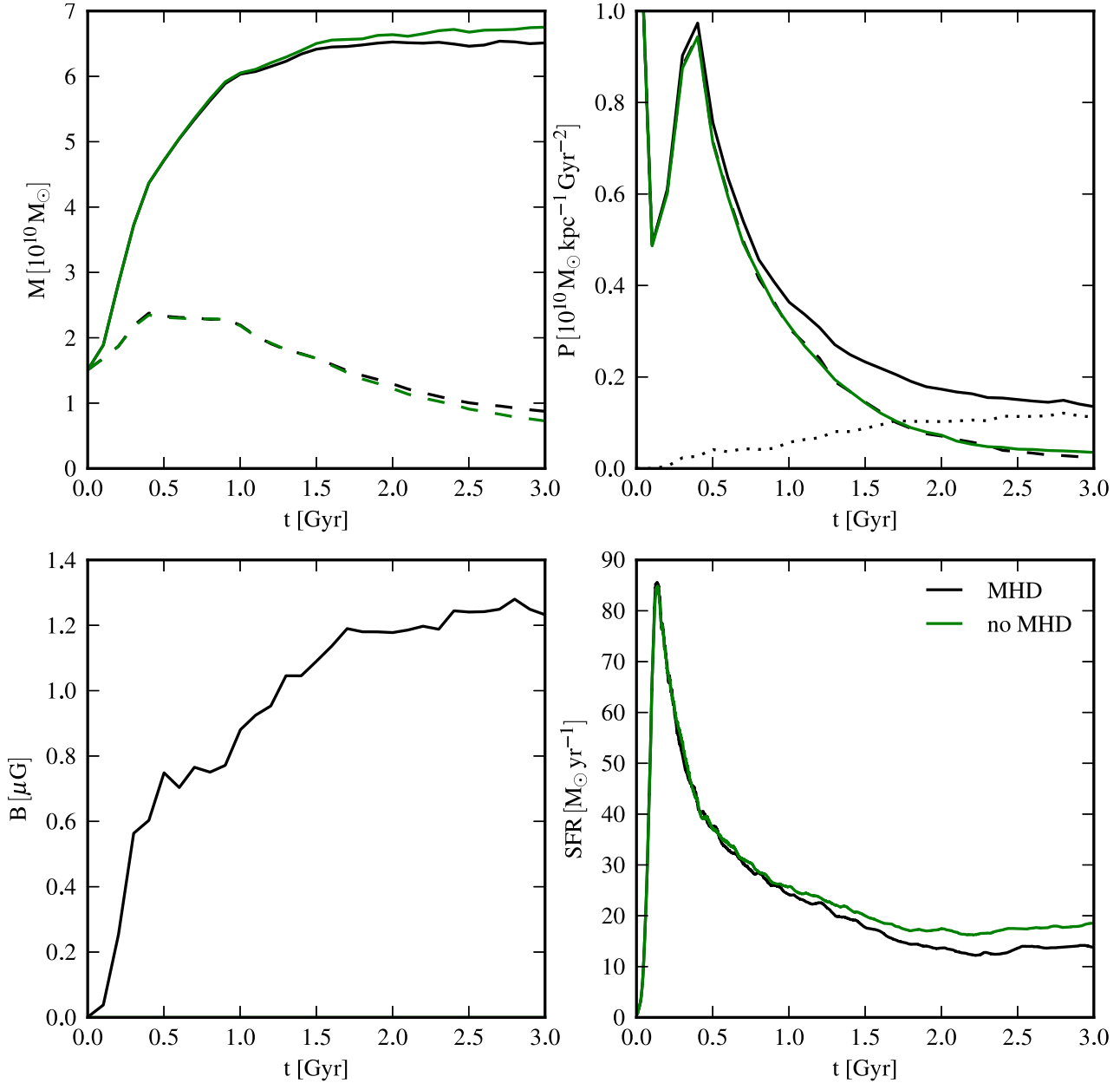


Figure 6. Time evolution of different quantities of a $10^{12} M_{\odot}$ galaxy with (black lines) and without magnetic field (black lines) for a mass resolution of $2.1 \times 10^5 M_{\odot}$. The top left panel shows the total baryonic mass in stars and gas (straight line) and the gas mass (dashed line) within a radius of 15 kpc. The top right panel shows the thermal pressure (dashed line), the magnetic pressure (dotted line) and the total pressure (straight line). The pressure is calculated as volume-weighted average in a sphere of radius 15 kpc around the center of the galaxy. The bottom left panel contains the volume-weighted average root mean square of the absolute value of the magnetic field within a radius of 15 kpc. Finally, the bottom right panel shows the total star formation rate in the whole simulation.

simulations. In this mode, the mesh-generating points, which define the Voronoi cells, are moved with the local fluid velocity, subject to small corrections to keep the shape of cells reasonably regular. In addition, we use refinement and derefinement operations where needed to ensure that the mass of the cells always stays within a certain narrow range: if a cell contains more than twice or less than half of the desired average mass per cell, we split it into two cells or merge it with its neighbours, respectively. The refinement and derefinement operations are carried out as described in Springel (2010) and Vogelsberger et al. (2012).

The gas is allowed to cool radiatively, which eventually causes the rotating gas sphere to develop a strong cooling flow and to form a rotationally supported disk inside-out at the centre. For simplicity, we only include atomic cooling by helium and hydrogen, ignoring molecules or metals. Therefore, the gas can only cool down to a temperature of 10^4 K. We include star formation and supernova feedback by means of a simple sub-resolution model (Springel & Hernquist 2003). This model assumes that star formation and associated supernova feedback lead to a self-regulated multiphase interstellar medium in which cold molecular clouds are

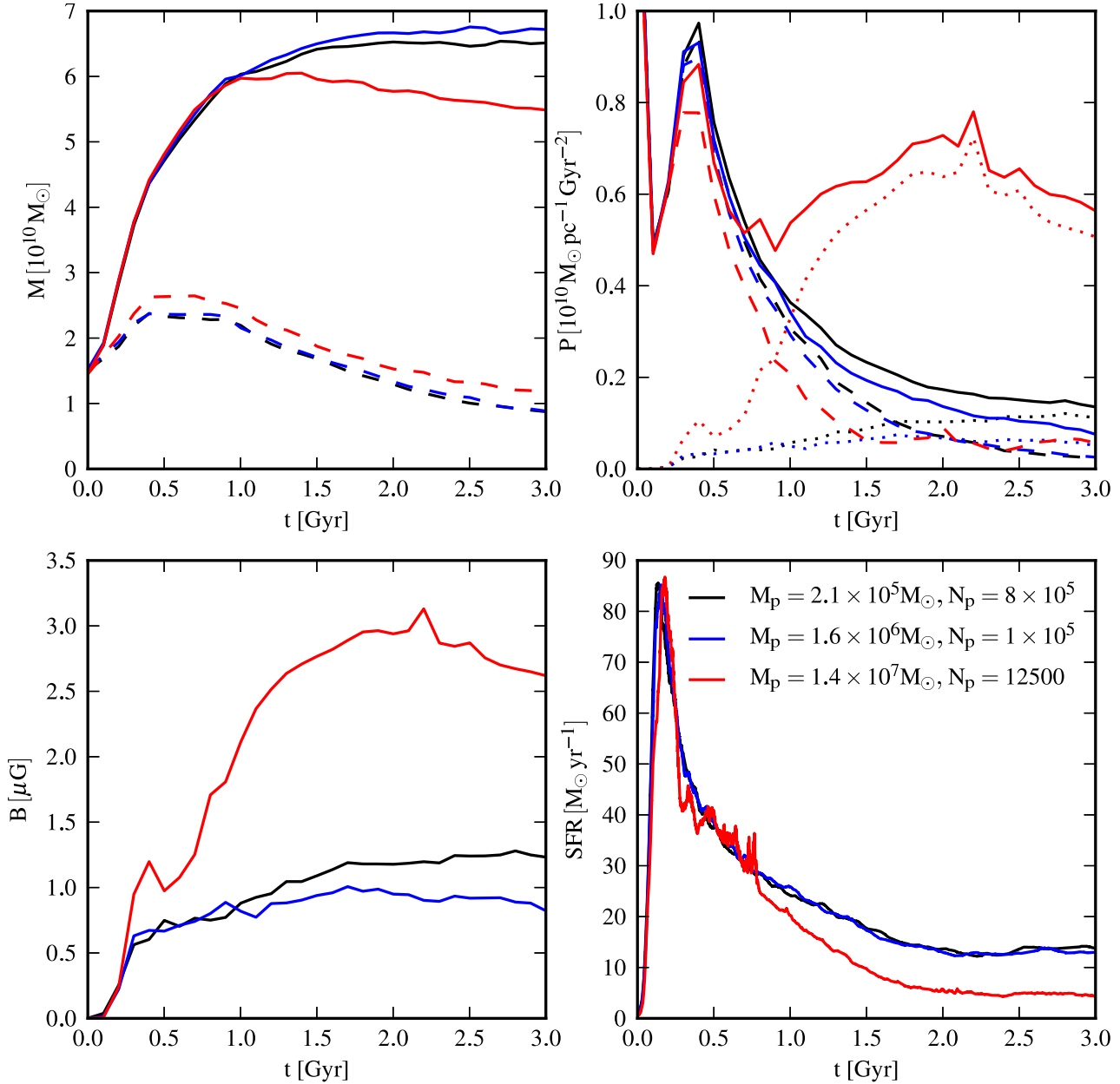


Figure 7. Resolution dependence of different quantities in simulations of a galaxy with a seed magnetic field of 10^{-9} G. Shown are simulations with a mass resolution of $2.1 \times 10^5 M_{\odot}$ (black lines), $1.6 \times 10^6 M_{\odot}$ (blue lines), and $1.4 \times 10^7 M_{\odot}$ (red lines). The top left panel shows the total baryonic mass in stars and gas (straight line) and the gas mass (dashed line) within a radius of 15 kpc. The top right panel shows the thermal pressure (dashed line), the magnetic pressure (dotted line) and the total pressure (straight line). The pressure is calculated as volume-weighted average in a sphere of radius 15 kpc around the center of the galaxy. The bottom left panel contains the volume-weighted average root mean square of the absolute value of the magnetic field within a radius of 15 kpc. Finally, the bottom right panel shows the total star formation rate in the whole simulation box.

embedded in a tenuous hot phase roughly at pressure equilibrium. The pressurization of the medium due to supernova feedback can be described by an effective equation of state. Stars are formed in a probabilistic approach out of the medium, with a gas consumption time-scale consistent with the observed Kennicutt (1998) relation for star-forming disk galaxies in the local Universe. Once a star is formed from a cell, we remove 90% of the mass, momentum and internal energy of the cell and create a collisionless star particle at the position of the cell that inherits the removed

mass and momentum. Since the cell only retains 10% of its mass, often a derefinement of the cell is triggered in the next timestep, meaning that the cell will be dissolved and its contents merged with its neighbors.

We do not include any local supernova feedback in the form of point-like energy depositions. Such local supernova feedback would likely increase the amplification of the magnetic field, because of the implied additional shearing motions and the higher turbulence in the interstellar medium.

Also, we do not change the magnetic field of a cell when

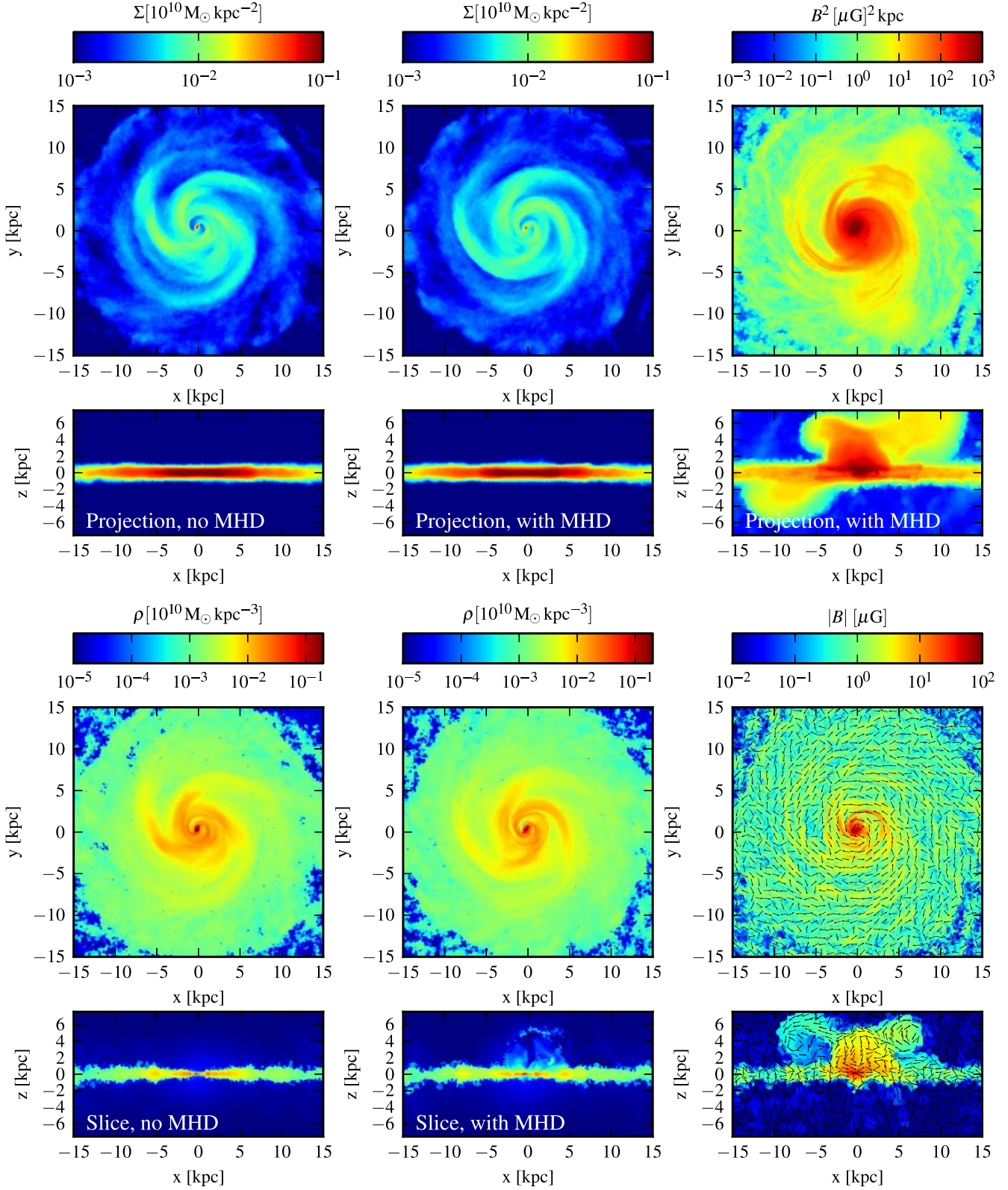


Figure 8. Gas density and magnetic field at $t = 1$ Gyr. Top two rows show projections, bottom rows slices through the center of the galaxy. The left column shows the density for the simulation with a mass resolution of $2.1 \times 10^5 M_{\odot}$ without a magnetic field. Center and left column show density and magnetic energy (for the projection) and magnetic field (on the slice) for the simulation with the same resolution but an initial magnetic seed field of 10^{-9} G.

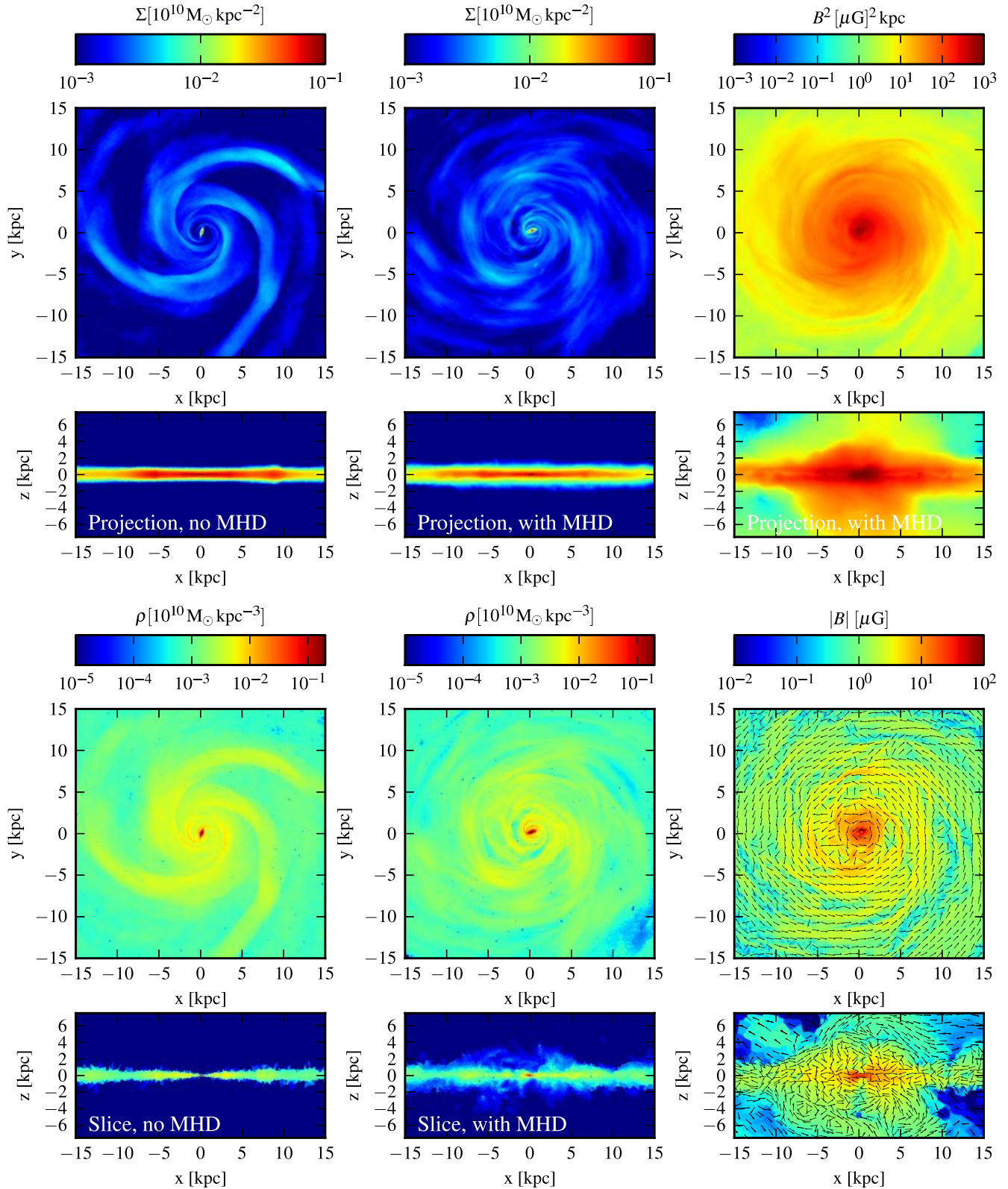


Figure 9. Gas density and magnetic field at $t = 2$ Gyr. The two rows on top show projections, the bottom rows slices through the center of the galaxy. The left column depicts the density for the simulation with a mass resolution of $2.1 \times 10^5 M_{\odot}$ without a magnetic field. Center and left column show density and magnetic energy (for the projection) and magnetic field (on the slice) for the simulation with the same resolution but an initial magnetic field of 10^{-9} G.

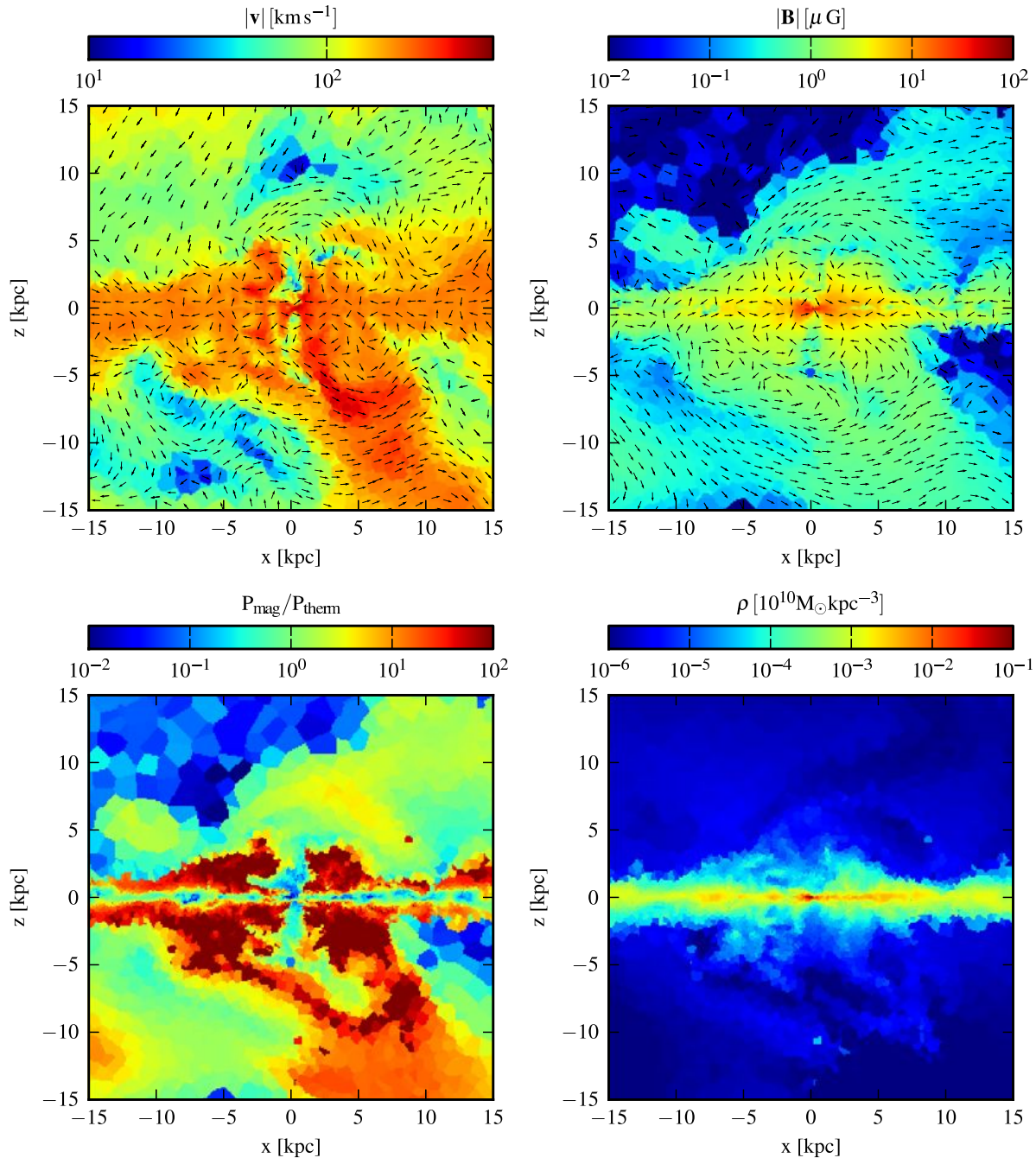


Figure 10. Properties of outflows above and below the disk at $t = 2$ Gyr for the simulation with a mass resolution of $2.1 \times 10^5 M_{\odot}$ with a magnetic field. Shown are the magnitude of the velocity (top left panel), the magnitude of the magnetic field (top right panel), the ratio of magnetic pressure to thermal pressure (bottom left panel) and the density (bottom right panel) in slices perpendicular to the disk.

a star is formed, similar to Dubois & Teyssier (2010) in their AMR-code. This has the major advantage that the local structure of the magnetic field is not affected by a star-forming event, and in particular, the divergence of the magnetic field does not increase when a star is formed. Note, however, that this is a conservative and non-trivial assumption. For the mass resolution we can afford, each “star particle” is a macro-particle that represents a whole stellar population formed in a molecular cloud. In such a cloud, magnetic fields can be strongly amplified by turbulence. At the same

time, some part of the magnetic field is locked up in stars, whereas another part is pushed out of the cloud by ambipolar diffusion. Therefore, the field dynamics in star-forming clouds is complicated and in reality it may well be possible that the magnetic field surrounding a molecular cloud is amplified during star formation. Similarly, but arguably less likely, it is possible that a molecular cloud leaves a smaller magnetic field behind after being depleted by star formation.

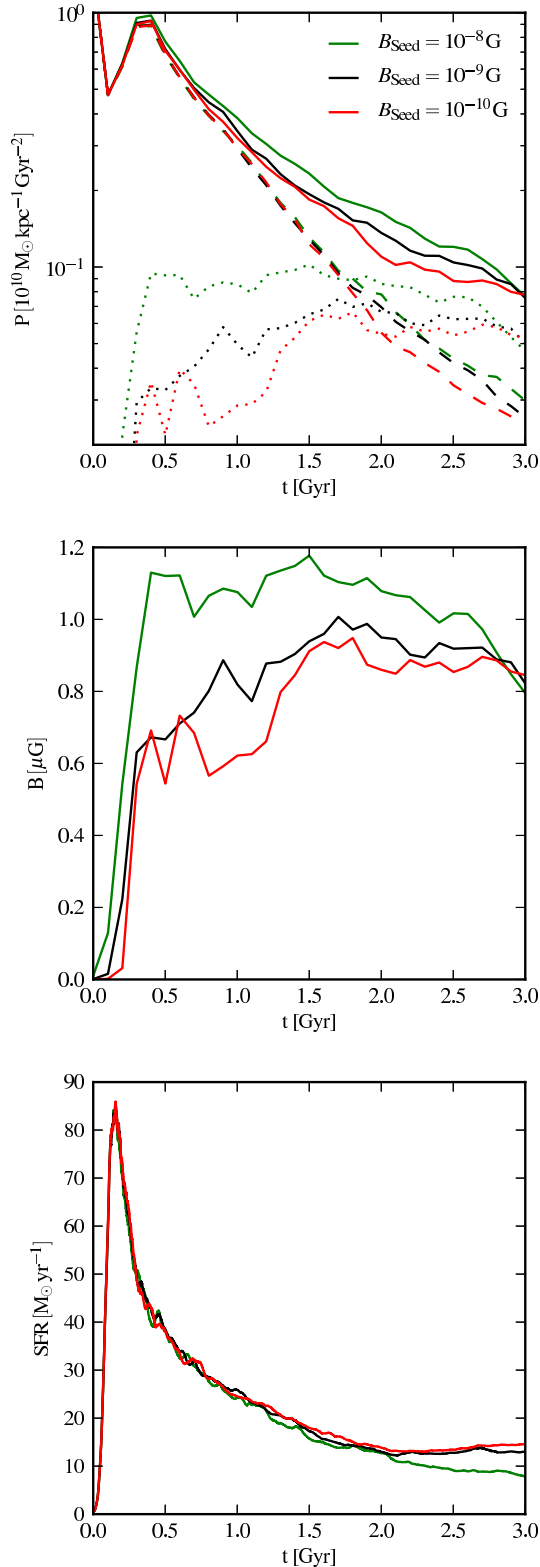


Figure 11. Time evolution of the pressure (top panel), the magnetic field (middle panel) and the star formation rate (bottom panel) for galaxies with seed magnetic fields from 10^{-8}G to 10^{-10}G . The straight, dashed and dotted lines in the top panel show volume-averaged total, thermal and magnetic pressure, respectively.

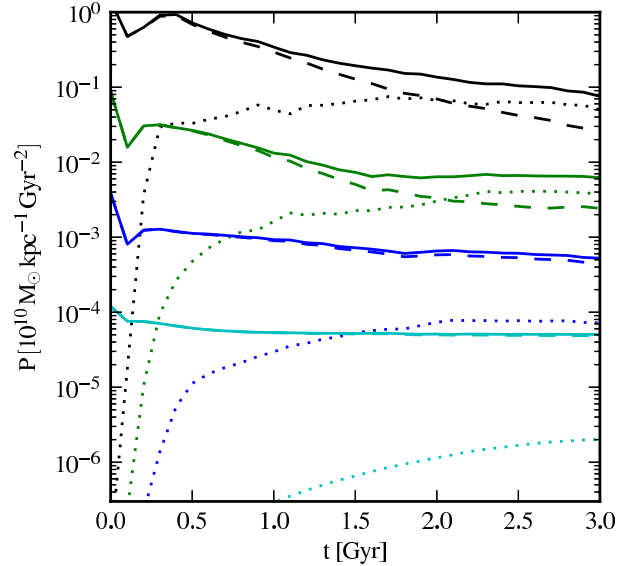


Figure 12. Time evolution of the volume-averaged total pressure (straight lines), thermal pressure (dashed lines) and magnetic pressure (dotted lines). Black, green, blue and cyan lines represent galaxies with halo masses of $10^{12} M_{\odot}$, $10^{11} M_{\odot}$, $10^{10} M_{\odot}$, and $10^9 M_{\odot}$, respectively.

5 DISK GALAXY RESULTS

Without radiative cooling, the initial gas spheres in our simulations remain in hydrostatic equilibrium. However, as we allow the gas to cool, the pressure support in the centre is removed and the gas sphere collapses. Since gas elements carry some angular momentum, they settle into a dense, rotationally supported disk that can locally fragment and form stars. The result is the formation of a disk galaxy in a classic inside-out fashion (Fall & Efstathiou 1980). Similar numerical experiments have frequently been used to study models of star formation and feedback (e.g. Springel & Hernquist 2003; Jubelgas et al. 2008). Here, we are primarily interested in whether magnetic fields can impact the dynamics of this disk formation scenario.

5.1 Global evolution

The global evolution of two galaxies with and without a magnetic seed field is compared in Figure 6. For the first 1.5 Gyrs the evolution is quite similar. After only about 200 Myrs the inner part of the gas sphere has collapsed and formed a small disk in which a large starburst has ensued. In this starburst, the star formation rate peaks just below $100 M_{\odot} \text{yr}^{-1}$, but drops to about $10 - 20 M_{\odot} \text{yr}^{-1}$ within a few hundred million years, at which point a more or less constant, only slowly declining star formation rate is reached.

The magnetic field is strongly amplified in the initial collapse of the gas cloud and the first starburst, from an initial field strength of 10^{-9}G to an average field strength of the order of μG in the inner parts, in agreement with observational constraints (Beck 2007). Much of the subsequent amplification proceeds through an Ω -type dynamo, made effi-

cient through the continued radial gas inflow combined with strong differential shear. The magnetic field saturates at the level of few μG , and no significant further amplification takes place in our simulation in places where the magnetic field has saturated. Once it has been amplified to this saturation level, we find that it also contributes significantly to the total pressure. Owing to the additional magnetic pressure, it becomes slightly harder for the gas to form stars. Therefore, as shown in Fig. 6, the star formation rate is lowered by about 30% at late times in the simulation with magnetic fields, compared to the run without magnetic fields. At late times, after more than 1.5 Gyrs, the average magnetic pressure even begins to dominate the average thermal gas pressure in parts of the star-forming gas disk.

5.2 Resolution dependence

Before we proceed with further analysis, we investigate the convergence of our results with numerical resolution. To this end, we have run the simulation with magnetic field at three different resolutions, using mass resolutions of $2.1 \times 10^5 M_\odot$, $1.6 \times 10^6 M_\odot$, and $1.4 \times 10^7 M_\odot$, respectively. The evolution of the galaxy for these different resolutions is compared in Figure 7.

The two higher resolution runs agree fairly well with each other. In particular, the magnetic field saturates at about the same value and it takes about the same time to reach saturation. In the lowest resolution simulation, however, the magnetic field is amplified somewhat faster, and saturates at an average value that is about a factor of three larger compared to the higher resolution runs. The magnetic pressure in this simulation also takes over the thermal pressure earlier (at about $t = 1$ Gyr) and the ratio of average magnetic pressure over average thermal pressure is significantly larger than unity. This finally leads to a considerably stronger suppression of star formation, and a late-time star formation rate of about one tenth of the late-time star formation rates in the high-resolution runs.

These differences suggest that in the low resolution run the amplification of the magnetic field is artificially increased due to poor resolution, caused in particular by relatively large divergence errors (see Fig. 13). We note however that the impact of these errors on the amplification is very much smaller than in the SPH calculations of Kotarba et al. (2009), where order of magnitude differences were found for different approaches to control the divergence errors. In contrast to our results, Dubois & Teyssier (2010) have found slightly smaller amplification for poor resolution, perhaps as a result of their accurate suppression of divergence errors. For isolated galaxies, the weak systematics we see in our technique for low resolution is not a serious problem, because such models can nowadays be simulated with at least the medium resolution we use here. In cosmological simulations of structure formation where galaxies form hierarchically, the reduced accuracy at low resolution is potentially a more serious concern. Here, the simulations always contain small progenitor galaxies which are initially resolved only with typically very few cells. Accurately capturing the dynamics of these systems when magnetic fields are involved may be quite challenging with our techniques.

5.3 Structure of the gas disk and its magnetic field

Projections of the gas density in the disk and maps of its magnetic field are shown in Figures 8 and 9, after one and two Gyrs, respectively. After one Gyr, the inner part of the gas halo has collapsed to a disk galaxy and converted a large fraction of its gas into stars. The structure of the galaxy at this time is very similar for the simulations with and without magnetic field. Even the position and morphology of individual spiral arms are very similar, and there is no difference in the thickness of the disks. This is consistent with the result that the magnetic pressure is on average still subdominant at this time, and therefore magnetic fields are not expected to have a substantial effect on the dynamics of the gas yet.

In the calculation with magnetic fields, the field has been amplified to maximum values of up to $100 \mu\text{G}$ in the center of the disk and to a few μG in its outer parts. The strength of the magnetic field is correlated with the spiral arms, with a significantly larger magnetic field in spiral arms than in between arms (consistent with Kotarba et al. 2009). Compared to the smooth spirals arms seen in the density field, the magnetic field strength shows a more patchy appearance with alternating regions of larger and smaller magnetic field strength. Interestingly, although we do not include winds from supernovae, the simulation with magnetic fields locally shows highly magnetized outflows from the disk which also transport magnetic fields outwards. While overall the magnetic field in the disk is aligned with the spiral structure of the disk, it also shows a lot of field reversals, similar as in Dubois & Teyssier (2010). The field strength is about a factor of 10 larger in the central part of the disk compared to its outskirts. In the central part, where the timescale on which differential rotation in the disk amplifies the magnetic field is smaller, the magnetic field is also more regular. We note that the structure of the simulated magnetic field is in good agreement with observational data of spiral galaxies (Beck 2007; Jansson & Farrar 2012b).

After an elapsed time of two Gyrs, the differences between the galaxies simulated with and without magnetic fields have become larger. By this time, the total gas mass in the disk has dropped by about a factor of two, as a result of star formation and the reduced supply of gas cooling out of the halo. The galaxy without magnetic field still shows distinct spiral arms and also retains about the same thickness it had one Gyr earlier. In contrast, in the simulation with a magnetic field, the individual spiral arms have mostly disappeared to form a smoother disk with weaker residual spiral patterns. The magnetic field in the disk is now very regular and well aligned with the residual spiral structures of the disk. This change can be explained in terms of the longer differential rotation time in the outer parts of the disk. Now after 2 Gyrs, differential rotation had enough time to also amplify the magnetic field in the outer parts to saturation values. Only in the very center of the disk a significant radial component remains. Field reversals in the disk still exist but have become much less frequent compared to the structure of the magnetic field at time $t = 1$ Gyr. In addition, the gas disk is now noticeably thicker compared to the disk without magnetic fields, as a result of the magnetic pressure contribution.

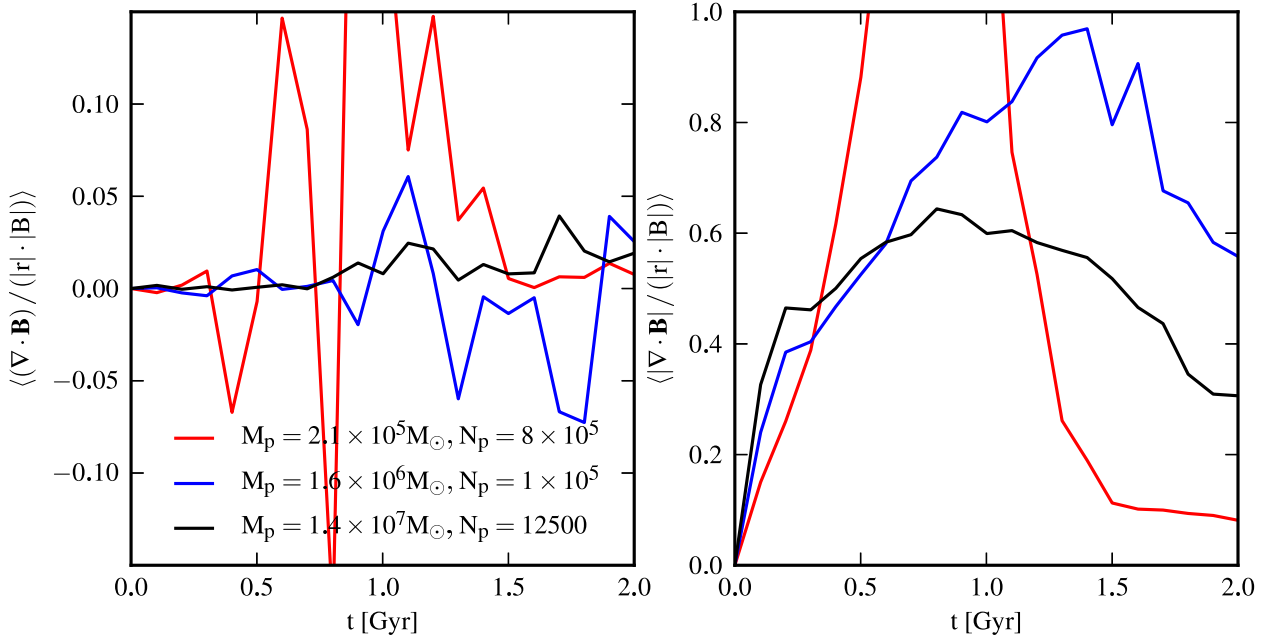


Figure 13. Time evolution of the relative divergence error of the magnetic field for the simulations with a mass resolution of $2.1 \times 10^5 M_\odot$ (black lines), $1.6 \times 10^6 M_\odot$ (blue lines), and $1.4 \times 10^7 M_\odot$ (red lines). Left and right panels show the volume-weighted average divergence error and the volume-weighted average *absolute* divergence error.

The magnetic field is primarily amplified by two processes in our simulations. In the first few 100 Myrs (during the initial starburst), adiabatic compression of the magnetic field dominates the amplification. As material cools, it becomes denser until its density reaches the star formation threshold. Then it forms stars and leaves a highly amplified magnetic field behind. Therefore, the magnetic field strength is initially correlated with the local star formation and is highest at the center of the disk, where the compression and the star formation rate is highest. Later, after the total star formation in the disk has dropped significantly, the amplification of the magnetic field is dominated by shear motions in the differentially rotating disk combined with radial inflows. This leads to a pronounced inside out growth of the magnetic field in the disk, because the orbital timescales increase for larger radii. The relentless shearing of the magnetic field in the disk also make it ever more regular with time.

There are other processes which are likely important for the amplification of magnetic fields in galaxies but which are not included in our present simulations. Because we evolve an isolated galaxy, it does not experience any large-scale shearing motions caused by infalling material or mergers with other galaxies that could lead to an additional amplification of the magnetic field. In addition, our subresolution model for the interstellar medium does not directly resolve interstellar turbulence, because we include supernova feedback smoothly through an effective equation of state (see Sec. 4). Therefore, we miss a possible turbulent amplification of the magnetic field on small scales.

In addition, we do not explicitly distinguish between neutral gas, which should not feel the magnetic field directly, and ionized gas, which interacts with the magnetic field. Instead, we neglect resistivity effects and treat all gas in the limit of ideal magnetohydrodynamics which will tend to

overestimate the dynamical effect of the magnetic pressure on the gas in the disk.

5.4 Outflows

The magnetized galaxy shows significant outflows of gas up to a few kpc above the disk and below the disk, as shown in Fig. 10. These outflows are strongly magnetized and their velocity vector is highly correlated with the magnetic field lines. We note that unlike in the simulations of Dubois & Teyssier (2010) these outflows are not driven by supernovae. While supernova feedback is implicitly included in our sub-resolution model for the ISM, it does not create galactic winds; instead its effects are absorbed in the applied effective equation of state.

The outflows are driven by low density, highly magnetized bubbles which rise above the disk. In our simulation they reach typical velocities of a few hundred km s^{-1} , almost reaching escape speed. The further they rise above the disk, the smaller their velocity and magnetic field becomes until they finally fall back onto the disk again. The outflows contain about $10^8 M_\odot$ of gas at $t = 2$ Gyr. Qualitatively, these outflows are similar to galactic fountain models in which outflows are driven by supernova-powered bubbles (see, e.g., Shapiro & Field 1976; Oosterloo et al. 2007; Marinacci et al. 2011). The quantitative properties of the outflows, however, have to be taken with care, since the resolution of our simulation is already rather low in these regions.

5.5 Varying the magnetic seed field

To understand the effect of the magnetic seed field on the evolution of the model galaxies, we repeat our simulation

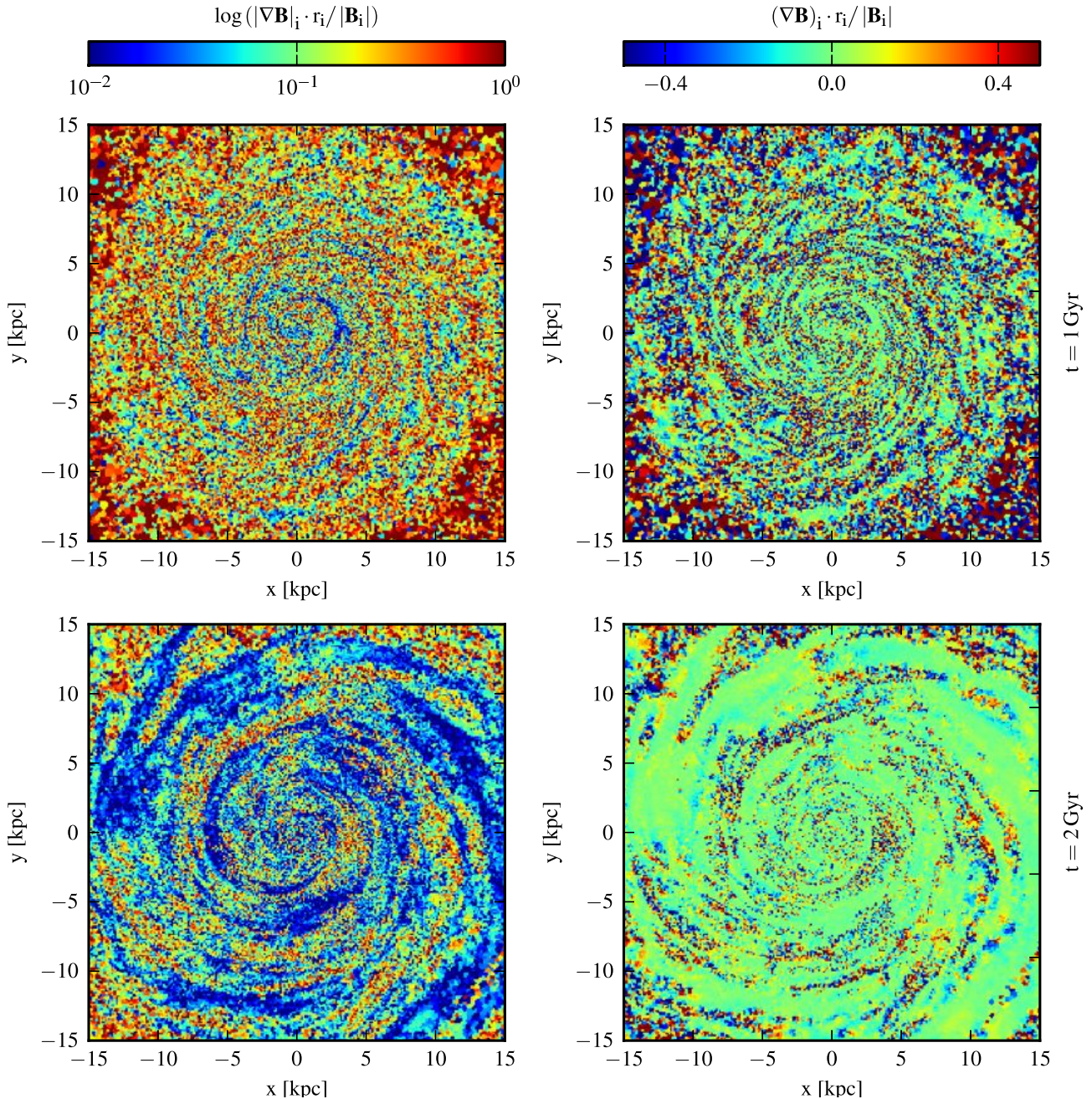


Figure 14. Relative divergence error of the magnetic field at $t = 10$ Gyr (top row) and at $t = 20$ Gyr (bottom row). The left column shows the absolute value of the relative divergence error, the right column shows the signed values.

with the intermediate resolution (which had a mass resolution of $1.6 \times 10^6 M_\odot$ and a seed field of 10^{-9} G) with a larger and a smaller seed field of 10^{-8} G and 10^{-10} G, respectively. The evolution of pressure, magnetic field and star formation rate compared to the original simulation is shown in Fig. 11.

Although the initial seed field differs by a factor of 10 compared with the original simulation, the evolution of the calculation with a ten times smaller seed field is hardly changed. In this case, the growth of the magnetic field is delayed by about 100 Myrs during the initial 300 Myrs. After this time, when the initial starburst subsides, the magnetic field in both simulations converges to the same value and

evolves basically identically, indicating that the magnetic field saturated to a state independent of the initial seed field. Because even directly after the starburst the magnetic pressure is still too small compared with the thermal pressure to be of dynamical relevance, the different choice of the seed field in this case does not affect the evolution of the galaxy or the evolution of the magnetic field once it is saturated.

The behavior of the simulation with a larger magnetic seed field of 10^{-8} G, however, is slightly different. After the initial starburst, the magnetic field is temporarily about twice as large as in the original simulation (where a seed field of 10^{-9} G was used). From this time onwards, it stays

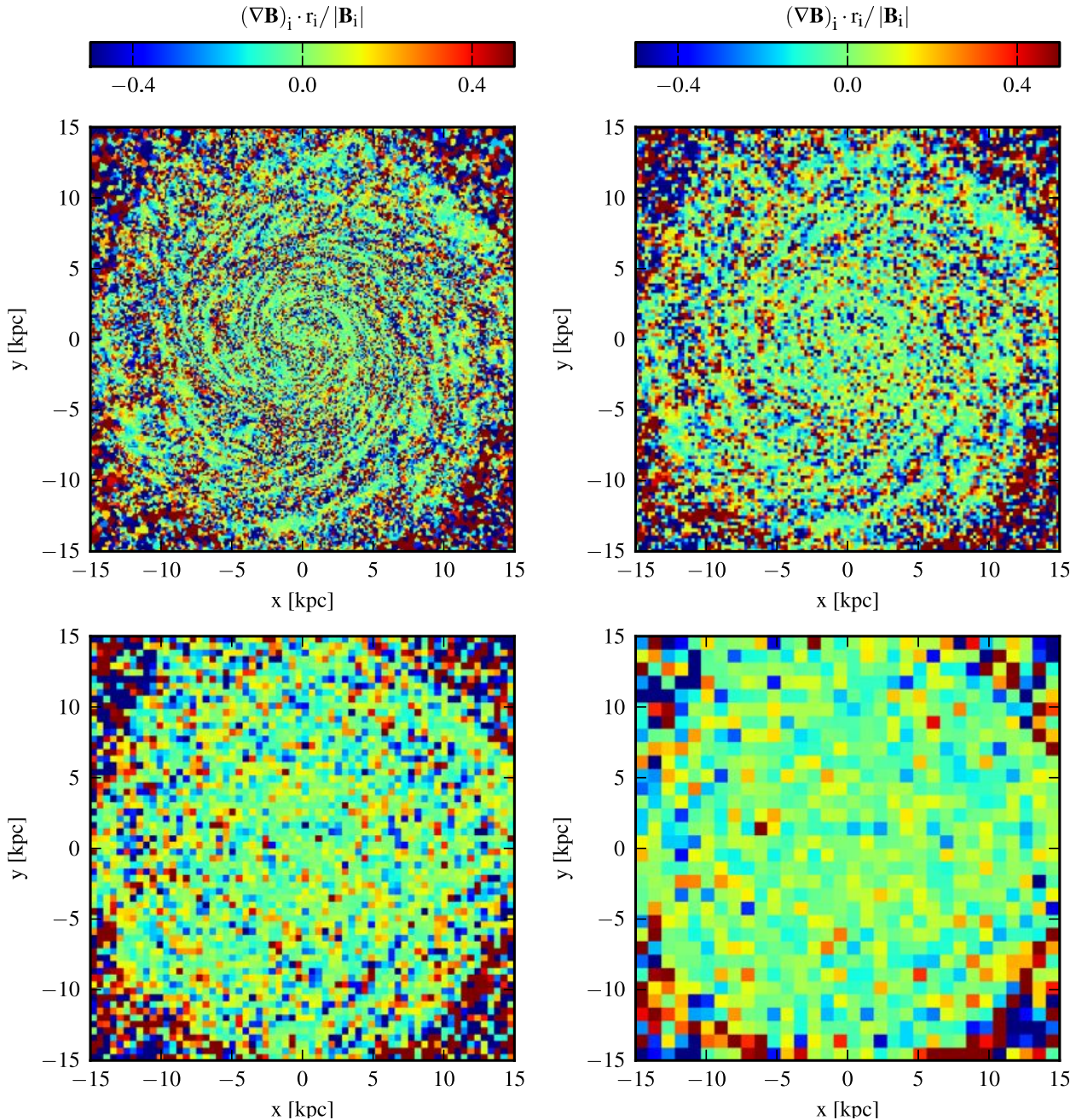


Figure 15. Relative divergence error of the magnetic field at $t = 10$ Gyr. The top left panel shows the error sampled on a 256×256 grid. Top right, bottom left, and bottom right panel show the error from the top left panel averaged over 2×2 , 4×4 , and 8×8 cells. This averaging rapidly reduces the residual local errors, indicating that the errors are locally compensated and do not induce incorrect large-scale magnetic dynamics.

roughly constant for two Gyrs at an elevated level until it finally decreases to the same strength as in the other two simulations that started with one or two order of magnitude weaker seed fields. Again, since the magnetic pressure is much smaller than the thermal pressure during the initial starburst and for most of the following time, this difference has only a small effect on the total pressure or the star formation rate. Only at late times, just before the magnetic field decreases to the value found in the other simulations, the star formation rate is suppressed slightly more than for

the other two calculations with smaller seed fields. We hence find that the saturation strength of the magnetic field is almost completely insensitive to the initial seed strength, apart from residual differences stemming from the different times required for amplifying the field from the initial strength to saturation.

5.6 Halos of different masses

Another important parameter in our simulations is the mass of the simulated galaxy. To complement our set of simulations, we have run three more simulations with 10^5 gas cells, with the total mass of the halo set to $10^{11} M_{\odot}$, $10^{10} M_{\odot}$, and $10^9 M_{\odot}$, respectively, and an initial magnetic field strength of 10^{-9} G. The virial radii of the halos were scaled in a self-similar fashion.

In Figure 12, we show the evolution of the average pressure in the galaxies forming in these simulations and compare it to our fiducial simulation with a halo mass of $10^{12} M_{\odot}$. The most important difference lies in the relative strength of the magnetic pressure developing for galaxies of different mass. For the two simulations with halo masses of $10^{12} M_{\odot}$ and $10^{11} M_{\odot}$, the magnetic pressure reaches equality with the thermal pressure after about two Gyrs. However, for the two lower mass galaxies, the magnetic field never becomes dynamically important. This difference from self-similar behavior is to be expected because of the non-self-similarity of cooling and star formation physics. Both the cooling efficiency and the ability of a halo's gravitational potential well to compress the gas of the interstellar medium against the pressure delivered by supernovae vary strongly with halo mass. In the lower mass halos, the potentials become too shallow for compressing the gas to very high densities, therefore the amplification of the magnetic field by adiabatic compression of the seed field is weaker. Furthermore, the much more anemic and thicker gas disks developing in these halos reduce the amplification of the magnetic field by differential shear. We thus expect that magnetic fields are particularly important only for those halos that are also efficient sites of star formation. According to recent abundance matching constraints for the Λ CDM cosmology (Guo et al. 2010; Moster et al. 2010), these are primarily halos in the mass range $\sim 10^{11.5-12.5} M_{\odot}$.

In the simulations with the $10^{12} M_{\odot}$ and $10^{11} M_{\odot}$ galaxies, outflows are present as discussed in Section 5.4, but they are absent in the two low mass galaxies with halo masses of $10^9 M_{\odot}$ and $10^{10} M_{\odot}$. This directly confirms that these outflows only occur once the magnetic field becomes dynamically important. We stress that these outflows are not caused by supernova feedback, rather they can form when the magnetic field pressure dominates over the thermal pressure of the gas in at least parts of the disk.

5.7 Divergence error

As discussed in Sec. 2.3, our discretization scheme of the MHD equations does not manifestly maintain a vanishing divergence of the magnetic field to machine precision; rather a finite divergence may appear, with the scheme preventing its further growth. Although such small divergence errors do not cause any obvious artifacts even in complex environments (including technically dicey steps such as de-refinement and star formation), it is important to examine the properties of the divergence error in more detail. We note that at the very least it can alter the local jump conditions for the Riemann solver, which in principle can sometimes lead to locally incorrect fluxes, causing larger numerical noise or possibly more severe artifacts.

In Fig. 13, we show the evolution of the average relative

divergence error as a function of time for different numerical resolutions in our default halo. With increasing resolution the divergence error decreases, which indicates that it is dominated by local noise in the magnetic field. This is also consistent with the average divergence error being much smaller (by more than a factor of 10) than the average *absolute* divergence error.

The spatial distribution of the divergence error is shown in Figure 14. Here it can be seen directly that the sign of the divergence error is alternating locally on small scales. There are basically no coherent patches of multiple cells with only positive or negative divergence error. The magnitude of the divergence error follows the pattern of the spiral arms, which can be easily understood as a consequence of the divergence errors correlating with large gradients of the magnetic field. In other words, large (unresolved) gradients in the local magnetic field cause large divergence errors at the same place. With higher resolution, the gradients are resolved better and the divergence errors become smaller.

Another confirmation of the local nature of the divergence error can be inferred from Figure 15, where local spatial averages of the divergence error are shown. They quickly reduce the error to the sub-percent level for progressively larger smoothing regions. This suggests that non-zero errors in the field divergence do not introduce changes in the large-scale dynamics of the magnetic field. Note also that the sizes of the divergence errors seen in our simulations are smaller or at most of the same order than in cosmological MHD simulations carried out with the latest generation of SPH-MHD methods (Dolag & Stasyszyn 2009; Beck et al. 2012; Stasyszyn et al. 2012), which have similar properties regarding magnetic field divergence errors.

6 CONCLUSIONS

In this study, we have examined the magnetic field amplification in simple models of disk galaxy formation. Our goal has been to provide a first exploration of the potential impact of magnetic fields for the regulation of star formation in Milky Way-sized galaxies. We have chosen isolated galaxies in order to allow a study of the magnetic field evolution in a well-controlled setting, while still confronting our numerical scheme with all the technical challenges (such as dealing with star formation events and on-the-fly derefinements) it has to cope with in future cosmological applications.

Another important aspect of our study lies in testing our new MHD implementation in the moving-mesh code AREPO, which we extended to cosmological simulations of galaxy formation that account for radiative cooling and star formation. In contrast to our previous method (Pakmor et al. 2011), we here use an 8-wave formulation (Powell et al. 1999) for dealing with the divergence constraint of the magnetic field. This new implementation turns out to be much more robust, whereas our previous MHD code could sometimes become unstable in very dynamic environments unless very strict timestep constraints were imposed.

We have shown in this paper that our new scheme produces competitive results for test problems and is successful in keeping the divergence error small. We have demonstrated that our new code is able to simulate the magneto-rotational instability in disks without problems, and that the correct

linear growth rate is reproduced. Also, we have shown that the new implementation prevents any noticeable artifacts in simulations of disk formation.

For our simulations of isolated galaxy formation, we observe good convergence for the strength of the magnetic field, the magnetic pressure and the star formation rates, unless the resolution is very low. In particular, we obtain converged results for our two high resolution runs with mass resolutions of $2.1 \times 10^5 M_\odot$ and $1.6 \times 10^6 M_\odot$, corresponding to an initial resolution of 8×10^5 gas cells and 1×10^5 gas cells in the halo, respectively. The magnetic field saturates at a strength of about $10 - 100 \mu\text{G}$ in the very center of the disk in a Milky Way-sized halo of mass $10^{12} M_\odot$, and at a few μG in the main body of the disk. We find that the star formation rate and structure of the gas disk is very similar for our runs with and without magnetic fields until about 1 Gyr. Later, the magnetic pressure becomes comparable to the thermal pressure, providing additional support for the gas and reducing the star formation rate by about 30%. It also causes changes the structure of the disk, reducing the prominence of individual spiral arms as the additional magnetic pressure produces slightly more homogeneous disks. Interestingly, the magnetic field causes weak outflows from the disks which rise several kpc above the disk before their material falls back.

Simulations of halos with a reduced mass of $10^{11} M_\odot$ yield qualitatively very similar results. Here the magnetic field is also amplified to a saturation level, allowing it to affect the galaxy dynamics at late times. In contrast, small halos with masses of $10^{10} M_\odot$ and $10^9 M_\odot$ did not amplify the magnetic field up to equipartition with the thermal pressure, due to insufficient star formation and gas compression. This can be understood as a consequence of the shallow gravitational potential well and the modified cooling efficiency in these systems.

Our results underline the potentially very important role magnetic fields play in galaxy formation, especially in systems that have a high efficiency of star formation, as here the gas is compressed particularly strongly and the amplification through gas shearing motions and inflows tends to be strong, too. In such galaxies, magnetic fields of typical IGM strength are quickly amplified to saturation values, such that the initial seed field strength is of very limited importance and tends to be quickly forgotten. It will be very interesting to examine the influence of magnetic fields on forming galaxies in cosmological hydrodynamic simulations of structure formation, which we plan to study in future work. The present work has demonstrated that such calculations are technically feasible and sufficiently accurate with our present MHD implementation in AREPO.

ACKNOWLEDGEMENTS

R.P. gratefully acknowledges financial support of the Klaus Tschira Foundation. V.S. acknowledges support by the DFG Research Centre SFB-881 ‘The Milky Way System’ through project A1.

REFERENCES

- Arshakian T. G., Beck R., Krause M., Sokoloff D., 2009, *A&A*, 494, 21
- Balbus S. A., Hawley J. F., 1991, *ApJ*, 376, 214
- Barnes J., Hut P., 1986, *Nature*, 324, 446
- Beck A. M., Lesch H., Dolag K., Kotarba H., Geng A., Stasyszyn F. A., 2012, *MNRAS*, 422, 2152
- Beck R., 2007, *A&A*, 470, 539
- Beck R., 2009, *Astrophysics and Space Sciences Transactions*, 5, 43
- Beck R., Brandenburg A., Moss D., Shukurov A., Sokoloff D., 1996, *ARA&A*, 34, 155
- Broderick A. E., Chang P., Pfrommer C., 2012, *ApJ*, 752, 22
- Carilli C. L., Taylor G. B., 2002, *ARA&A*, 40, 319
- Cox D. P., 2005, *ARA&A*, 43, 337
- Dedner A., Kemm F., Kröner D., Munz C., Schnitzer T., Wesenberg M., 2002, *Journal of Computational Physics*, 175, 645
- Dolag K., Bartelmann M., Lesch H., 1999, *A&A*, 348, 351
- Dolag K., Bartelmann M., Lesch H., 2002, *A&A*, 387, 383
- Dolag K., Stasyszyn F., 2009, *MNRAS*, 398, 1678
- Dubois Y., Teyssier R., 2010, *A&A*, 523, A72
- Evans C. R., Hawley J. F., 1988, *ApJ*, 332, 659
- Fall S. M., Efstathiou G., 1980, *MNRAS*, 193, 189
- Flock M., Dzyurkevich N., Klahr H., Mignone A., 2010, *A&A*, 516, A26
- Govoni F., Feretti L., 2004, *International Journal of Modern Physics D*, 13, 1549
- Guo Q., White S., Li C., Boylan-Kolchin M., 2010, *MNRAS*, 404, 1111
- Hanasz M., Kowal G., Otmianowska-Mazur K., Lesch H., 2004, *ApJ*, 605, L33
- Ipavich F. M., 1975, *ApJ*, 196, 107
- Jansson R., Farrar G. R., 2012a, *ArXiv e-prints*, 1204.3662
- Jansson R., Farrar G. R., 2012b, *ArXiv e-prints*, 1210.7820
- Jubelgas M., Springel V., EnBlin T., Pfrommer C., 2008, *A&A*, 481, 33
- Kennicutt Jr. R. C., 1998, *ApJ*, 498, 541
- Kitchatinov L. L., Rüdiger G., 2004, *A&A*, 424, 565
- Kotarba H., Karl S. J., Naab T., Johansson P. H., Dolag K., Lesch H., Stasyszyn F. A., 2010, *ApJ*, 716, 1438
- Kotarba H., Lesch H., Dolag K., Naab T., Johansson P. H., Donnert J., Stasyszyn F. A., 2011, *MNRAS*, 415, 3189
- Kotarba H., Lesch H., Dolag K., Naab T., Johansson P. H., Stasyszyn F. A., 2009, *MNRAS*, 397, 733
- Kronberg P. P., Lesch H., Hopp U., 1999, *ApJ*, 511, 56
- Kulsrud R. M., 1999, *ARA&A*, 37, 37
- Kulsrud R. M., Zweibel E. G., 2008, *Reports on Progress in Physics*, 71, 046901
- Marinacci F., Fraternali F., Nipoti C., Binney J., Ciotti L., Londrillo P., 2011, *MNRAS*, 415, 1534
- Miyoshi T., Kusano K., 2005, *Journal of Computational Physics*, 208, 315
- Moster B. P., Somerville R. S., Maulbetsch C., van den Bosch F. C., Macciò A. V., Naab T., Oser L., 2010, *ApJ*, 710, 903
- Narayan R., Medvedev M. V., 2001, *ApJ*, 562, L129
- Navarro J. F., Frenk C. S., White S. D. M., 1997, *ApJ*, 490, 493
- Neronov A., Vovk I., 2010, *Science*, 328, 73

- Oosterloo T., Fraternali F., Sancisi R., 2007, *AJ*, 134, 1019
Pakmor R., Bauer A., Springel V., 2011, *MNRAS*, 418, 1392
Parker E. N., 1979, *Cosmical magnetic fields: Their origin and their activity*. Oxford, Clarendon Press; New York, Oxford University Press
Powell K. G., Roe P. L., Linde T. J., Gombosi T. I., de Zeeuw D. L., 1999, *Journal of Computational Physics*, 154, 284
Robishaw T., Quataert E., Heiles C., 2008, *ApJ*, 680, 981
Shapiro P. R., Field G. B., 1976, *ApJ*, 205, 762
Springel V., 2005, *MNRAS*, 364, 1105
Springel V., 2010, *MNRAS*, 401, 791
Springel V., Hernquist L., 2003, *MNRAS*, 339, 289
Staszczyn F. A., Dolag K., Beck A. M., 2012, *ArXiv e-prints*, 1205.4169
Strong A. W., Moskalenko I. V., 1998, *ApJ*, 509, 212
Vogelsberger M., Sijacki D., Kereš D., Springel V., Hernquist L., 2012, *MNRAS*, 425, 3024
Wang P., Abel T., 2009, *ApJ*, 696, 96
Zweibel E. G., Heiles C., 1997, *Nature*, 385, 131